23 Jan 2023

Direct Synthesis of Ethylene and Hydrogen from CO2 and Ethane over a Bifunctional Structured CaO/Cr2O3-V2O5/ZSM-5 Adsorbent/Catalyst Monolith

Khaled Baamran

Ali A. Rownaghi

Fateme Rezaei
Missouri University of Science and Technology, rezaeif@mst.edu

Recommended Citation

K. Baamran et al., "Direct Synthesis of Ethylene and Hydrogen from CO2 and Ethane over a Bifunctional Structured CaO/Cr2O3-V2O5/ZSM-5 Adsorbent/Catalyst Monolith," *ACS Sustainable Chemistry and Engineering*, vol. 11, no. 3, pp. 1006 - 1018, American Chemical Society, Jan 2023.
The definitive version is available at https://doi.org/10.1021/acssuschemeng.2c05627

ACS Sustainable Chemistry & Engineering

pubs.acs.org/journal/ascecg

Research Article

Direct Synthesis of Ethylene and Hydrogen from CO_2 and Ethane over a Bifunctional Structured CaO/Cr_2O_3-V_2O_5/ZSM-5 Adsorbent/Catalyst Monolith

Khaled Baamran, Ali A. Rownaghi,* and Fateme Rezaei*

Cite This: *ACS Sustainable Chem. Eng.* 2023, 11, 1006−1018

Read Online

ACCESS | Metrics & More | Article Recommendations | Supporting Information

ABSTRACT: In this study, we synthesized bifunctional adsorbent/catalyst materials (BFMs) consisting of a CaO adsorbent admixed with Cr_2O_3-V_2O_5/ZSM-5 catalysts. The obtained BFMs were further formulated, processed, and shaped through additive manufacturing (3D printing) method. The physical and chemical properties of structured CaO/Cr_2O_3-V_2O_5/ZSM-5 adsorbent/catalyst monoliths were thoroughly characterized and evaluated. The effects of operating conditions including reaction temperature, ethane composition, and space velocity on single-bed CO_2 capture and selective formation of ethylene and hydrogen were systematically investigated. The adsorption−reaction experiments revealed that Cr-based BFMs, in particular, CaO/Cr_4/ZSM-5 monoliths undergo the oxidative dehydrogenation pathway with high C_2H_4 selectivity, whereas increasing the content of V leads to enhanced catalytic activity for the reforming pathway to produce hydrogen. The best adsorption/catalyst BFM performance was observed for CaO/Cr_1-V_3/ZSM-5, which was balanced between the two reaction pathways and resulted in 1.72 mmol/g CO_2 capture capacity, 63.95% CO_2 conversion, 22.4% C_2H_6 conversion, 42% C_2H_4 selectivity, and 45% syngas (31% hydrogen) selectivity. Furthermore, the cyclic test results revealed excellent catalytic stability across the initial two cycles over CaO/Cr_1-V_3/ZSM-5 monolith, highlighting the synergetic effect of bimetallic catalyst constituents on maintaining high catalytic durability. This novel formulation and processing method can pave the way toward formulation of various structured BFM monoliths with cooperative CO_2 adsorptive removal and catalytic performance for one-pot CO_2 capture−utilization and simultaneous production of light olefins and hydrogen.

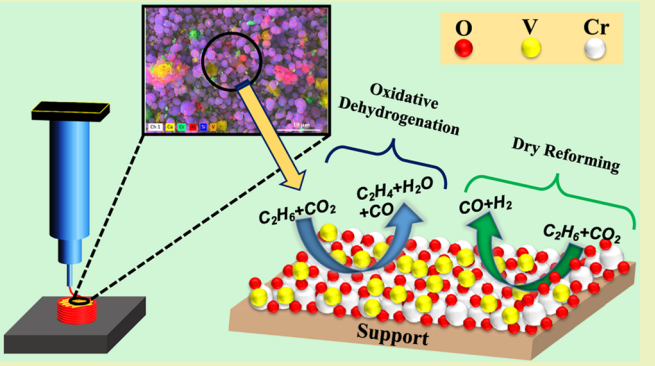

KEYWORDS: *bifunctional adsorbent/catalyst materials, additive manufacturing (3D printing), in situ CO_2 capture−utilization, oxidative dehydrogenation of ethane, hydrogen production*

INTRODUCTION

Ethylene (C_2H_4) is an important raw feedstock used to produce diverse chemicals such as polyethylene oxide, polyethylene, vinyl acetate, and ethylene dichloride. The typical process used for C_2H_4 production is the steam cracking of hydrocarbons such as naphtha, which occurs at high temperatures (750−950 °C).[1−3] The global demand for C_2H_4 has increased dramatically in recent years and it is anticipated that C_2H_4 supply will not meet the future demand, thus development of novel processes technologies for sustainable production of C_2H_4 is crucial to meet such ever-increasing demands.[4] In that regard, the ubiquitous presence of C_2H_6 in shale gas makes the process of direct C_2H_6 dehydrogenation to C_2H_4 a promising approach from an economic point of view. However, the route of direct dehydrogenation usually leads to catalyst deactivation due to active metal sintering and coke formation, which makes it economically unviable due to frequent catalysts regeneration requirements.[5,6]

Another route for enhancing the catalyst stability and achieving high C_2H_6 conversion is utilizing CO_2 as a mild oxidant in the reaction of C_2H_6 dehydrogenation. The presence of CO_2 reduces the coke deposition formed on the catalyst surface *via* the Boudouard reaction, thereby maintaining the catalyst stability.[7] Also, the oxidative dehydrogenation of C_2H_6 with CO_2 (CO_2-ODHE) can enhance the C_2H_6 equilibrium conversion via the reverse water gas shift reaction (RWGS).[8] Furthermore, the presence of CO_2 in the ODHE reaction could lead to the production of hydrogen because the reaction of CO_2-ODHE has two main pathways: (i) oxidative

Received: September 22, 2022
Revised: December 1, 2022
Published: December 15, 2022

https://doi.org/10.1021/acssuschemeng.2c05627
ACS Sustainable Chem. Eng. 2023, 11, 1006−1018

dehydrogenation and (ii) dry reforming.[9] The latter reaction produces syngas via the scission of the C−C bond (e.g., H_2 and CO), while the former reaction yields C_2H_4 via the cleavage of the C−H bond.[10−12] Thermodynamic assessments have suggested that both reactions can occur simultaneously at temperatures greater than 550 °C, yielding the products of dehydrogenation and reforming reactions.[13] In this regard, developing active and cost-effective catalysts for increasing the reaction rate of both reactions is highly desirable due to the beneficial applications of C_2H_4 and hydrogen.[14]

As attractive as this idea is, CO_2 needs to be first captured and stored before utilization to use as a feedstock. The capture of CO_2 is carried out in a totally separate adsorption system, followed by a subsequent reaction process. The adsorption step typically takes place at temperatures below the reaction step, resulting in a large temperature swing between the two steps.[15,16] This situation leads to long cycle times due to additional cooling and heating steps.[17−19] Such issues can be resolved by operating both adsorption and reaction steps isothermally or close to isothermal conditions. This novel technique can minimize the need to store and transport CO_2, thus making the process of combining CO_2 capture and utilization an attractive route from economic and industrial perspectives.[18,20]

In that regard, utilizing materials comprising of adsorptive and catalytic phases (i.e., bifunctional materials (BFMs)) offers a promissing approach to perform CO_2 adsorption−reaction steps in a single bed, thereby lowering the thermal gradient requirements. It has been theorized that BFMs can reduce the thermal energy penalties compared to segregated systems of adsorption and reaction, which require higher energy for heating two columns as opposed to heating one column. However, design and development of such BFMs with optimized adsorption-reaction performance is a daunting challenge.[18,21,22] As an example of using BFMs for *in situ* CO_2 capture-utilization in ODHE, we previously synthesized various BFMs consisting of CaO, which works as the adsorption phase for CO_2 capture via high-temperature reaction to $CaCO_3$,[23] and Cr/ZSM-5 as the heterogeneous catalytic phase.[15,24] Under optimal adsorption−reaction conditions (e.g., adsorption = 600 °C and reaction = 700 °C), 4 mmol/g CO_2 uptake capacity, 42.5% C_2H_6 conversion, 38.6% C_2H_4 yield, and 90.6% C_2H_4 selectivity were achieved over these BFMs. We later formulated these BFMs into monolithic structures using 3D printing, and investigated their CO_2 adsorption-reaction performance.[25−33] The formulated BFM monoliths exhibited enhanced catalytic activity at high channel density (i.e., cell per square inch or cpsi) but at the expense of lower adsorptive performance due to pore blockage, which was stemmed from binders interlocking with the adsorption particles, affecting the adsorption site accessibility.[32]

The metal alloying strategy has been reported as an effective way to enhance the catalyst stability and activity.[34] In particular, precious/transition metal catalysts supported on porous substrates have been widely investigated in the CO_2-ODHE reaction, where these catalysts were often alloyed with other metals to improve their catalytic longevity and activity.[35,36] Chen *et al.* studied transition and transition/precious bimetallic catalysts (e.g., FeNi/CeO_2, CoPt/CeO_2, etc.) in CO_2-ODHE reaction and found that bimetallic catalysts displayed higher activity and stability compared to their corresponding monometallic catalysts.[37] The type of constituent metal elements plays a key role in improving the product selectivity. For example, the FeNi bimetallic catalyst was shown to facilitate the oxidative dehydrogenation pathway to C_2H_4, while its monometallic counterpart preferably followed the dry reforming route to syngas selectivity. This different catalytic behavior was attributed to the bimetallic interfaces and CO_2 regulation of oxygen species availability, which are responsible for changing the reaction route. In a similar study but for propane dehydrogenation, Ryoo *et al.*[38] investigated bimetallic catalysts comprising of Pt alloyed with rare earth metals and supported on zeolite as a mesoporous support containing pore walls with abundancy of oxygen species on the surface. They found that Pt-rare earth bimetals were stable and very selective toward reaction pathway of propane dehydrogenation to propylene compared to PtLa and PtSn. The enhanced stability of bimetallic catalysts and selectivity toward a certain reaction route were attributed to the synergetic effect between metals, and the presence of CO_2, which regulated the oxygen surface coverage to hinder coke formation and retain catalyst durability. Despite promisses, the precious metals are undesirable for industrial applications due to their rarity and high cost.

Most recently, we investigated several BFMs comprising of transition metal oxides supported on mesoporous zeolite (ZSM-5) and combined with a high-temperature adsorbent (CaO).[31,39,40] We showed that Cr_2O_3 was the most selective toward C_2H_4, while the other metal oxides (e.g., V_2O_5) enhanced the catalytic activity toward the production of CO and H_2. Therefore, in this study, we came up with a new set of monolithic BFMs consisting of Cr alloyed with V as bimetallic catalysts, supported on ZSM-5, and combined with CaO adsorbent to enhance the catalytic activity toward both oxidative dehydrogenation and dry reforming reactions to produce C_2H_4 and hydrogen. The metal ratio between Cr and V was varied to find the optimum synergetic interaction between them. The oxygen species availability was systematically investigated for the best bimetallic BFM and compared with that of its monometallic BFM counterpart . The operating conditions such as reaction temperature (600, 625, and 650 °C), weight hourly space velocity (WHSV) (1800, 3000, or 4200 mL/g·h), and C_2H_6 feed concentration (2.5, 5, and 10%) were varied to determine their influence on catalytic performance and stability of the best monolithic BFM (Cr_1-V_4/ZSM-5/CaO). Overall, this study provides important insights on development and formulation of dual function materials with bimetallic catalytic phases for use in CO_2 capture-utilization processes.

EXPERIMENTAL SECTION

Materials. The following materials were used for the BFMs synthesis without further purification: chromium oxide (Cr_2O_3, 98%), vanadium oxide (V_2O_5, 98%), calcium carbonate ($CaCO_3$, 99%), bentonite clay (99%), methylcellulose (99%), and ZSM-5 (SiO_2/Al_2O_3 ratio = 280). All these chemicals were purchased from Sigma-Aldrich except ZSM-5, which was obtained from Zeolyst International. The ultrahigh purity (UHP) gases used in this study were obtained from Airgas.

Structured BFM Monolith Formulation, Processing, and Formation. The monoliths were 3D-printed using techniques outlined in our previous works with the paste compositions shown in Table 1.[31,32] Briefly, the various paste components were suspended in ∼15−20 mL of DI water as depicted in Figure 1, sonicated for 30 min, and rolled for 48 h at 60 rpm to generate binding and achieve homogeneity. The obtained slurry was mixed at 600 rpm under

https://doi.org/10.1021/acssuschemeng.2c05627
ACS Sustainable Chem. Eng. 2023, 11, 1006−1018

Table 1. Paste Composition of 3D-Printed BFM Monoliths

monolith	Cr_2O_3 (wt %)	V_2O_5 (wt %)	ZSM-5 (wt %)	$CaCO_3$ (wt %)	bentonite (wt %)	methyl cellulose (wt %)
ZC			45	45	7	3
Cr_4/ZC	4		43	43	7	3
Cr_3-V_1/ZC	3	1	43	43	7	3
Cr_2-V_2/ZC	2	2	43	43	7	3
Cr_1-V_3/ZC	1	3	43	43	7	3
V_4/ZC		4	43	43	7	3

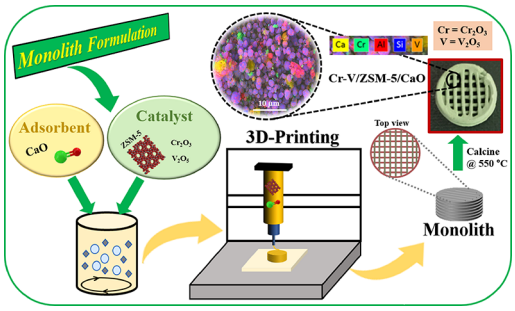

Figure 1. Schematic representation of the 3D printing steps followed for formulation of structured BFM monoliths.

heating (~50 °C) for 2−3 h to evaporate water and attain a printable rheology. This step was to extract water until a self-standing rheology was observed, where the self-standing behavior is defined as retaining layer separation after printing without fluidic spreading. The formed paste was filled into a syringe, in which a suitable pressure was applied to extrude the paste into a desired monolith shape. The printed monoliths were then dried at room temperature to prevent cracking for 12 h, thereafter they were calcined in air at 550 °C using a heating rate of 10 °C/min for 6 h to achieve strong mechanical stability and reduce the structure shrinkage that may have occurred at high temperatures (ca. above 550 °C). The BFM monoliths developed, namely, CaO/ZSM-5, CaO/Cr_4/ZSM-5, CaO/Cr_3-V_1/ZSM-5, CaO/Cr_2-V_2/ZSM-5, CaO/Cr_1-V_3/ZSM-5, and CaO/V_4/ZSM-5, were labeled as ZC, Cr_4/ZC, Cr_3-V_1/ZC, Cr_2-V_2/ZC, Cr_1-V_3/ZC, and V_4/ZC, respectively, where Cr = Cr_2O_3 and V = V_2O_5.

Structured BFM Monolith Characterization. The textural properties of the monoliths were assessed by N_2 physisorption on a Micromeritics (3Flex) gas analyzer at 77 K. A Micromeritics Smart VacPrep instrument was used to degas the samples before analysis at 350 °C for 6 h. After analysis, the pore size distribution (PSD) and surface area were estimated by the nonlocal density functional theory (NLDFT) and Brunauer−Emmet−Teller (BET) methods, respectively. The Cr and V oxidation states and metal dispersion in the printed monoliths were evaluated via X-ray photoelectron spectroscopy (XPS) on a Thermo Scientific Nexsa 128 channel XPS system, field emission scanning electron microscopy (FE-SEM), and energy dispersive spectroscopy (EDS) on a Quanta 600F ESEM with a Bruker Quantax EDS. To determine the functional groups, FT-IR experiments were carried out on a Nicolet Nexus 470 optical bench, while the redox properties were assessed on a 3Flex via temperature-programmed reduction in hydrogen (H_2-TPR). The catalytic acidities were assessed *via* temperature-programmed desorption of ammonia (NH_3-TPD). A Q500 thermogravimetric analyzer was used for coke formation analysis after the adsorption−reaction experiments. Therein, the surface of spent samples was cleaned by flowing 40 mL/min of N_2 at 900 °C using 25 °C/min ramp. The Raman spectra of the fresh and spent samples were collected with a μ-Raman spectrometer (ARAMIS; HORIBA Jobin Yvon Inc., Edison, NJ) using a He−Ne laser (632.8 nm).

***In Situ* CO_2 Capture−Utilization and Simultaneous Production of Ethylene and Hydrogen in a Single Bed.** The combined CO_2 capture−utilization experiments were performed using the system detailed in our prior work.[32] In a typical experiment, 0.5 g of the BFM was placed in the middle of the reactor, which was made of stainless steel with the dimensions of l.14 cm inner diameter and 22.8 cm height, between two layers of quartz wool. The samples were first pretreated by heating at 10 °C/min to 700 °C for 1 h under the 30 mL/min flowrate of Ar. The bed was subsequently cooled to the adsorption temperature (600 °C) and 25 mL/min of 10% CO_2/Ar was flowed into the reactor until saturation of CO_2 concentration was observed in the outlet. When the CO_2 concentration was plateaued, the flow of 10% CO_2/Ar was terminated, and simultaneously, the 25 mL/min flowrate of 5% C_2H_6/Ar was introduced into the system and the reactor was heated at a rate of 100 °C/min to reach 650 °C, as the typical reaction temperature in this study. The reaction was allowed to continue until the effluent CO_2 reached zero in concentration. It should be noted that most of the adsorption−reaction experiments were performed under our base conditions: 25 mL/min flowrate of 10% CO_2/Ar, 600 °C adsorption temperature, 25 mL/min flowrate of 5% C_2H_6/Ar, and 650 °C reaction temperature; however, the reaction temperature (600, 625, or 650 °C), WHSV (1800, 3000, and 4200 mL/g·h), and C_2H_6 feed concentration (2.5, 5, and 10%) were specifically changed for the best sample performance (Cr_1-V_3/ZC), as will be explained in the following sections. The effluent concentration profiles were collected using an MKS II Mass Spectrometer, and the product distribution was determined from the correlations detailed in our prior works and reported in the Supporting Information, eqs S1−S9.[15,24,32]

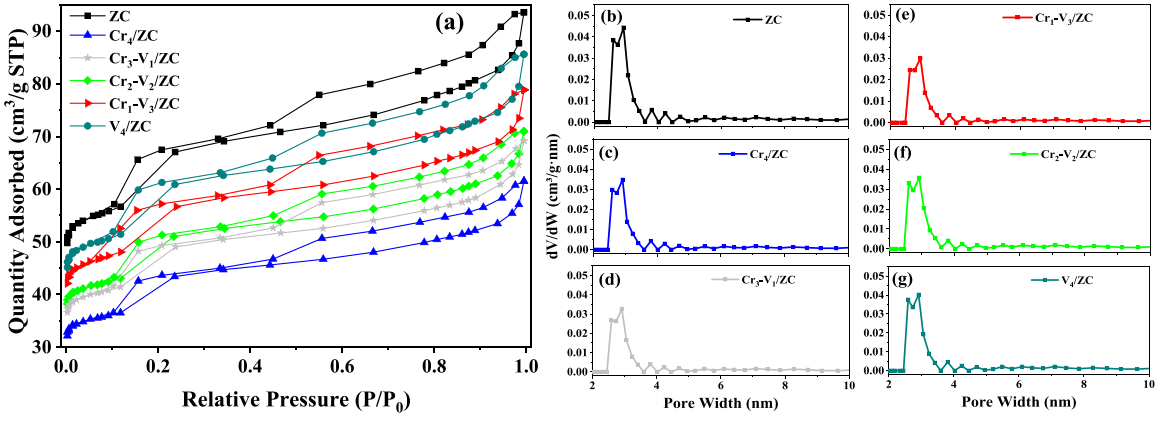

Figure 2. (a) N_2 physisorption isotherms and (b−g) PSD profiles of ZC and corresponding BFM monoliths.

https://doi.org/10.1021/acssuschemeng.2c05627
ACS Sustainable Chem. Eng. 2023, 11, 1006−1018

RESULTS AND DISCUSSION

Textural Properties of BFM Monoliths. The N_2 physisorption isotherms and the PSD profiles are shown in Figure 2a–g, and the textural properties are summarized in Table 2. In Figure 2a, the isotherms were characterized by a hysteresis loop (nearly horizontal and parallel branched curves) and a saturation plateau at $P/P_0 \sim 0.97$, which indicated the isothermal behavior of type IV and a hysteresis loop of type H4.[41,42] This hysteresis loop occurs due to a capillary condensation as the relative pressure is increased, indicating a mesoporous structure.[43] The obtained physisorption behaviors were expected because the control phase (ZC) possesses a mesoporous structure. The mesoporosity was further supported by the samples' PSD profiles, where the width was clearly observed to be larger than 2.5 nm. This conclusion is further supported by the samples' textural properties in Table 2, where the pore space of monoliths was allocated >2.5 nm, which is the mesoporous regime.[44] These findings were expected because the metal oxides and bentonite are known to be mesoporous.[27] Between the individual samples, the textural properties of the monolithic BFMs were essentially consistent; however, there were differences in the surface areas between the BFM monoliths, namely, Cr_4/ZC, V_4/ZC, and ZC, which were 147.7, 204.4, and 226.8 m^2/g, respectively, whereas the surface areas of Cr-V/ZC monoliths were in the range of 165–190 m^2/g. The reduction in the surface area stemmed from the larger particulate of Cr compared to V, which could block some of the ZSM-5 pores, as evidenced by the pore volume decline from 0.121 to 0.084 cm^3/g for these samples. Nevertheless, these results confirmed that BFMs retained the textural properties of ZC, further demonstrating that BFMs with monometallic or bimetallic catalyst phases can be printed into monolithic structures without malformation of the textural properties of the parent zeolite.

Table 2. Textural Properties of 3D-Printed BFM Monoliths

monolith	S_{BET} (m^2/g)	V_{micro} (cm^3/g)	V_{meso} (cm^3/g)	d_p (nm)
ZC	227	0.024	0.121	2.5, 2.7, 2.9, 3.1, 3.4, 3.6
Cr_4/ZC	148	0.011	0.084	2.5, 2.7, 2.9, 3.1, 3.4, 3.6
Cr_3-V_1/ZC	165	0.014	0.093	2.5, 2.7, 2.9, 3.1, 3.4, 3.6
Cr_2-V_2/ZC	174	0.013	0.097	2.5, 2.7, 2.9, 3.1, 3.4, 3.6
Cr_1-V_3/ZC	190	0.018	0.104	2.5, 2.7, 2.9, 3.1, 3.4, 3.6
V_4/ZC	204	0.016	0.116	2.5, 2.7, 2.9, 3.1, 3.4, 3.6

Surface Morphology of BFM Monoliths and Dispersion of Cr and V. The SEM images of Cr_4/ZC and Cr_1-V_3/ZC monoliths and their corresponding EDS maps are illustrated in Figure 3a–f and Figure 3g–l, respectively. By looking first at Figure 3a–f and then Figure 3g–k, it is clear that both samples displayed similar morphologies and metal (Ca, Si, Cr, and Al) dispersion. However, by comparing the active metal dispersion (Cr and V) in both samples, it was apparent that Cr existed in large pockets of Cr_2O_3 and produced stronger signals, indicating that Cr was available in larger particle sizes relative to V. On the other hand, V displayed small and more isolated pockets of V_2O_5, which are determined to exist in further extent at greater structural depth.[32] In this respect, the EDS images indicated that Cr_2O_3 as a monometallic catalyst could result in a better degree of metal oxide active sites accessibility, whereas the combination of the bimetallic constituents in the BFM could lead to better contact between the different active sites within the same catalyst.

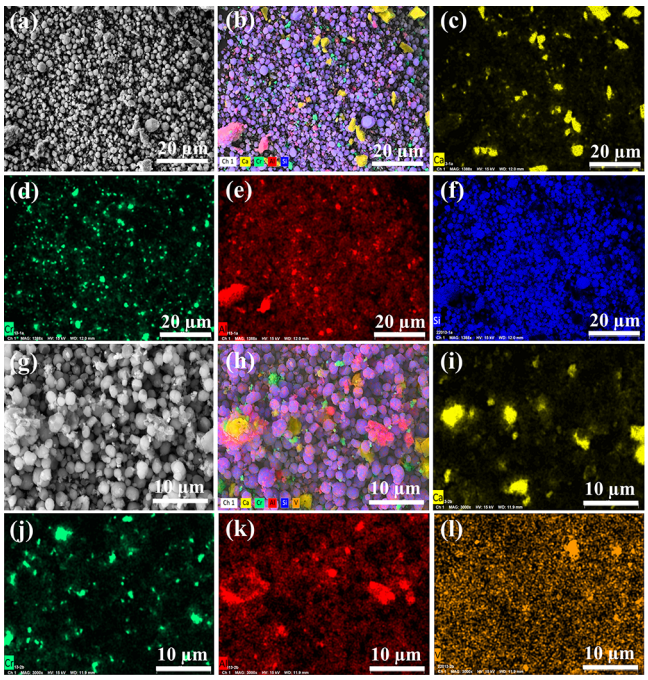

Figure 3. SEM-EDS of structured (a–f) Cr_4/ZC and (g–l) Cr_1-V_3/ZC monoliths.

Surface Acidities and Redox Properties of BFM Monoliths. The NH_3-TPD profiles of the 3D-printed BFM monoliths are depicted in Figure 4a, while the corresponding weak and strong acidic sites amounts are summarized in Table 3. The intensity refers to the NH_3 amount desorbed after pretreatment of the samples with NH_3. All the samples exhibited a broad peak in the range of 100–400 °C and another broad peak from 450 to 750 °C, indicating that all the samples possessed both weak and strong acid sites. The area under each peak is proportional to the number of the acid sites. All the monoliths showed an increased amount of weak and strong acid sites with similar peaks to the bare monolith (ZC); however, the peaks were shifted to higher temperatures in the BFM monoliths, implying that the strength of acid sites was increased by the metal modification in these monoliths. The highest concentration of strong acid sites existed in bimetallic modified monoliths, namely, Cr_1-V_3/ZC. The enhanced acidity of these monoliths can be ascribed to the doping of Cr_2O_3 and V_2O_5, as Cr and V are known to contain a high concentration of strong acid sites.[31,39,40] This was further supported by the increased peak intensity for Cr_1-V_3/ZC compared to ZC, which corresponded to the elevated compositions of Cr and V, as shown in Table 3. Therefore, based on the strong acid sites densities, the monoliths' acidities were approximated in the following order: Cr_1-V_3/ZC > Cr_2-V_2/ZC > V_4/ZC > Cr_3-V_1/ZC > Cr_4/ZC > ZC.

The FT-IR spectra of the printed BFM monoliths are shown in Figure 4b,c. The peaks at nearly 445 cm^{-1} were ascribed to the vibration of the internal Al–O or Si–O bonds in the form

https://doi.org/10.1021/acssuschemeng.2c05627
ACS Sustainable Chem. Eng. 2023, 11, 1006–1018

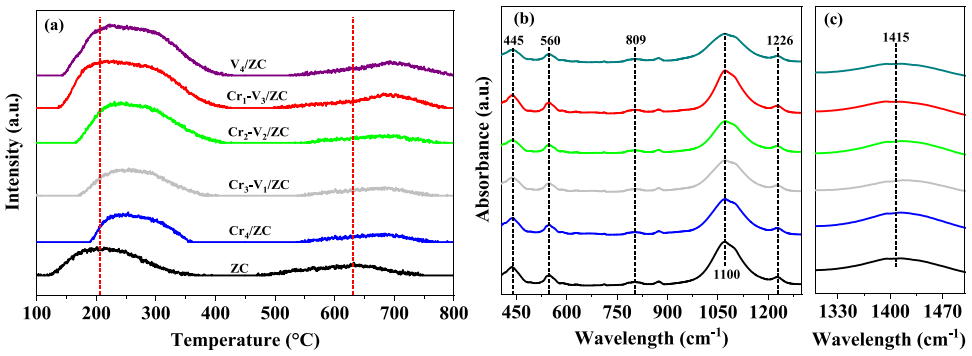

Figure 4. (a) NH_3-TPD profiles and (b, c) FT-IR spectra of the BFM monoliths.

Table 3. Density of Active Sites within BFM Monoliths Determined by NH_3-TPD

	weak acid area (T = 100−400 °C)		strong acid area (T = 450−750 °C)		
monolith	NH_3 desorption (mmol NH_3/g_{cat})	acid sites density ×10^4 (mmol/m^2)	NH_3 desorption (mmol NH_3/g_{cat})	acid sites density ×10^4 (mmol/m^2)	total acid sites density ×10^4 (mmol/m^2)
ZC	0.21	09.29	0.040	1.76	07.93
Cr_4/ZC	0.14	09.47	0.060	4.06	14.89
Cr_3-V_1/ZC	0.25	11.51	0.058	3.50	15.01
Cr_2-V_2/ZC	0.31	17.82	0.062	3.56	21.38
Cr_1-V_3/ZC	0.35	18.42	0.080	4.21	22.63
V_4/ZC	0.36	17.61	0.070	3.42	21.03

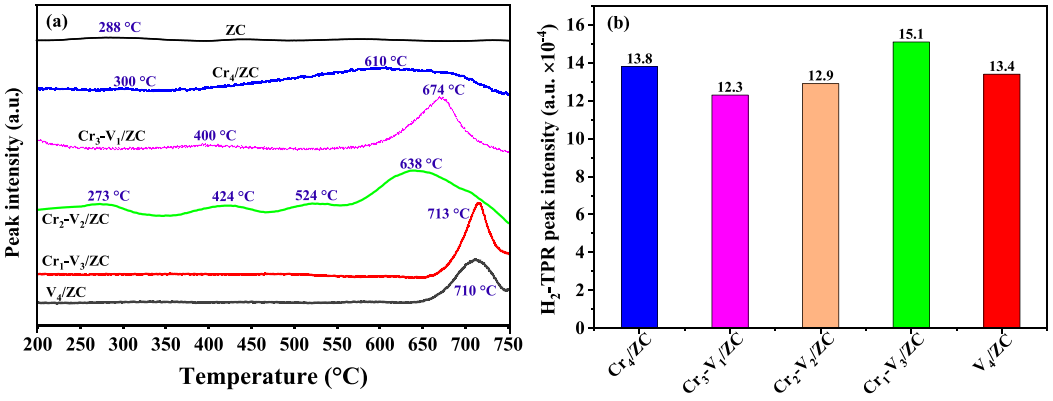

Figure 5. (a) H_2-TPR profiles and (b) H_2-TPR peak area intensity at temperatures above 600 °C for BFM monoliths.

of an AlO_4 or SiO_4 tetrahedron, which are the main metals in the zeolite framework.[45,46] The peaks observed at 560 cm^{-1} were related to the external bonds of double five-membered rings.[45] The bands appeared at about 810 cm^{-1} were associated with the symmetric stretching of external bonds between tetrahedra.[47] The peaks found around 1220 cm^{-1} were a reflection of the symmetric stretching vibration of Al−O or Si−O bonds due to the external linkages between AlO_4 and SiO_4 tetrahedra.[48] The most intense peak appeared at ∼1100 cm^{-1} was assigned to the internal asymmetric stretching bonds of Si−O−Si or Si−O−Al.[48] The broad band at 1415 cm^{-1} corresponded to the C−O bond and indicated CaO carbonation ($CaCO_3$), which was the precursor used for CaO.[49] There were no obvious peaks of Cr or V oxides due to the small compositions of these oxides in the formed monoliths.

The redox properties of the structured BFMs were evaluated by H_2-TPR, as illustrated in Figure 5. First, it should be noted here that the peaks displayed at temperatures below 300 °C were attributed to the H_2 reaction into water over −OH clusters in the zeolite. This reaction only occurs between the functional groups of −OH in ZSM-5 and does not stem from the reduction of ZSM-5, as reported in the literature.[27] In all of the Cr-containing samples, a peak was observed in the range of 610−624 °C, which could be ascribed to the reduction of bulk Cr_2O_3 into Cr species (e.g., Cr^{6+} and Cr^{3+}).[32] As the V content increased in the printed monoliths, the peaks were shifted to higher temperatures, suggesting the reduction of V_2O_5 into V species such as V^{5+} and V^{4+}, consistent with the literature.[27,50] This observation was also evidenced by the monometallic V-containing monolith. Moreover, the peaks that appeared at 400, 424, and 524 °C in the Cr_3-V_1/ZC and Cr_2-V_2/ZC samples could be ascribed to residual water desorption from the bentonite binder as these peaks had low intensity. As another possibility, these peaks were likely produced during alloying of Cr and V in the bimetallic monoliths.[27] Overall, the printed monoliths exhibited similar redox properties but the properties were affected slightly by varying the metals ratio a in the following order: Cr_1-V_3/ZC > Cr_4/ZC > V_4/ZC > Cr_2-V_2/ZC > Cr_3-V_1/ZC > ZC.

https://doi.org/10.1021/acssuschemeng.2c05627
ACS Sustainable Chem. Eng. 2023, 11, 1006−1018

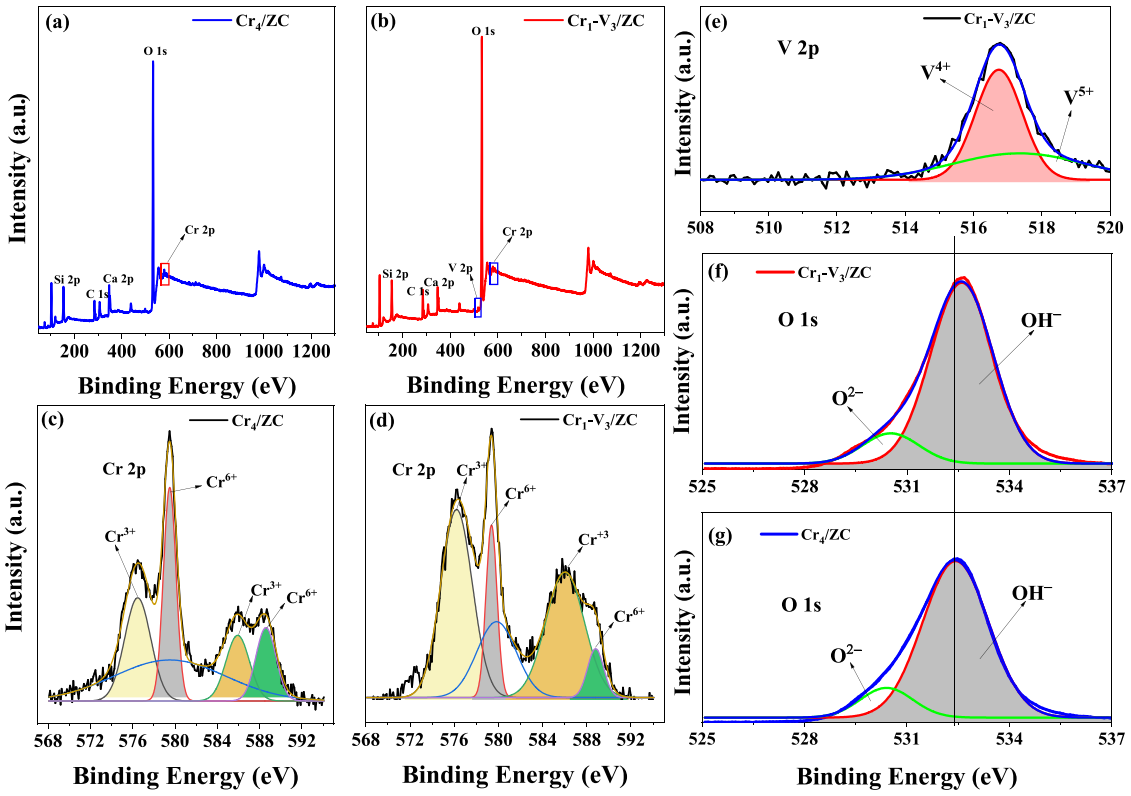

Figure 6. XPS spectra of BFM monoliths: (a, b) survey, and deconvoluted spectra of (c, d) Cr 2p, (e) V 2p, and (f, g) O 1s.

Table 4. XPS Results of Curve Fitting on Cr 2p and O 1s Binding Energies and Their Corresponding Species for BFM Monoliths

monolith	parameter	Cr $2p_{3/2}$			Cr $2p_{1/2}$			parameter	O 1s		
Cr_4/ZC	species	Cr^{3+}	Cr^{6+}	Cr^{6+}/Cr^{3+}	Cr^{3+}	Cr^{6+}	Cr^{6+}/Cr^{3+}	species	O^{2-}	OH^-	O^{2-}/OH^-
	BE (eV)	576.48	579.48	1.098	585.98	588.68	1.003	BE (eV)	530.4	532.4	0.39
	peak intensity (a.u.) $\times 10^{-4}$	2.79	3.07		2.77	2.78		peak intensity (a.u.) $\times 10^{-5}$	1.74	4.44	
Cr_1-V_3/ZC	species	Cr^{3+}	Cr^{6+}	Cr^{6+}/Cr^{3+}	Cr^{3+}	Cr^{6+}	Cr^{6+}/Cr^{3+}	species	O^{2-}	OH^-	O^{2-}/OH^-
	BE (eV)	576.48	579.48	1.042	585.98	588.68	0.993	BE (eV)	530.2	531.9	0.42
	peak intensity (a.u.) $\times 10^{-4}$	3.02	3.14		2.96	2.94		peak intensity (a.u.) $\times 10^{-5}$	2.07	4.92	

XPS analysis of Cr_4/ZC and Cr_1-V_3/ZC was performed to speculate the elemental composition, Cr and V oxidation states, and binding energies, as depicted in Figure 6. The XPS survey of Cr_4/ZC confirmed the presence of Si 2p, C 1s, Ca 2p, O 1s, and Cr 2p with their corresponding binding energies at 103, 284.5, 353.1, 532.4, and 585.5 eV, respectively, whereas the XPS survey of Cr_1-V_3/ZC confirmed the existence of the same elemental orbits, in addition to the elemental orbit of V 2p and its corresponding binding energy (BE) at 516.7 eV (Figure 6a,b). The high-resolution spectrum of Cr 2p was also obtained to investigate the effect of bimetals (Cr-V) on chromium oxidation states in Cr_1-V_3/ZC, and compared with the high-resolution spectrum of Cr 2p in Cr_4/ZC. For this, all the peaks in the range of Cr 2p for both samples were deconvoluted using the Gaussian method after subtracting the peaks from the baseline using the Shirley method. Cr 2p displayed two prominent peaks in the binding energy ranges of 572−581 and 582−590 eV, corresponding to Cr $2p_{3/2}$ and Cr $2p_{1/2}$, respectively. Each intense peak contained two oxidation states, namely, the hexavalent chromium ion (Cr^{6+}) and trivalent chromium ion (Cr^{3+}), as depicted in Figure 6c,d. The estimated ratio of Cr^{6+}/Cr^{3+} with their corresponding binding energies is shown in Table 4. Cr_4/ZC displayed relatively higher Cr^{6+}/Cr^{3+} ratio than Cr_1-V_3/ZC. However, the peak intensities were higher in Cr_1-V_3/ZC. In the ODHE reaction, Cr^{6+}/Cr^{3+} ratios and peak intensities play a key role in affecting the concentration of acid sites and redox properties, mainly due to the high electronic state of Cr^{6+}, thereby affecting the reaction products distribution.[24,32]

In Figure 6f,g, both samples displayed O 1s in the range of 529−536 eV but the oxygen peak intensity was higher in Cr_1-V_3/ZC and slightly shifted to a higher binding energy compared to that in Cr_4/ZC, as shown in Table 4, indicating the presence of more oxygen species on the surface of Cr_1-V_3/ZC, in agreement with the literature.[50] Therefore, O 1s, in both samples, was deconvoluted to determine the oxygen species. The signals between 530 and 536 eV were ascribed to the presence of oxygen lattice species (e.g., O^{2-}) and oxygen adsorption species (e.g., OH^-).[51,52] Table 4 shows the amounts of oxygen species and their corresponding binding energies. The high amount of oxygen species in Cr_1-V_3/ZC can be assigned to the high pore volume obtained by BET analysis

https://doi.org/10.1021/acssuschemeng.2c05627
ACS Sustainable Chem. Eng. 2023, 11, 1006−1018

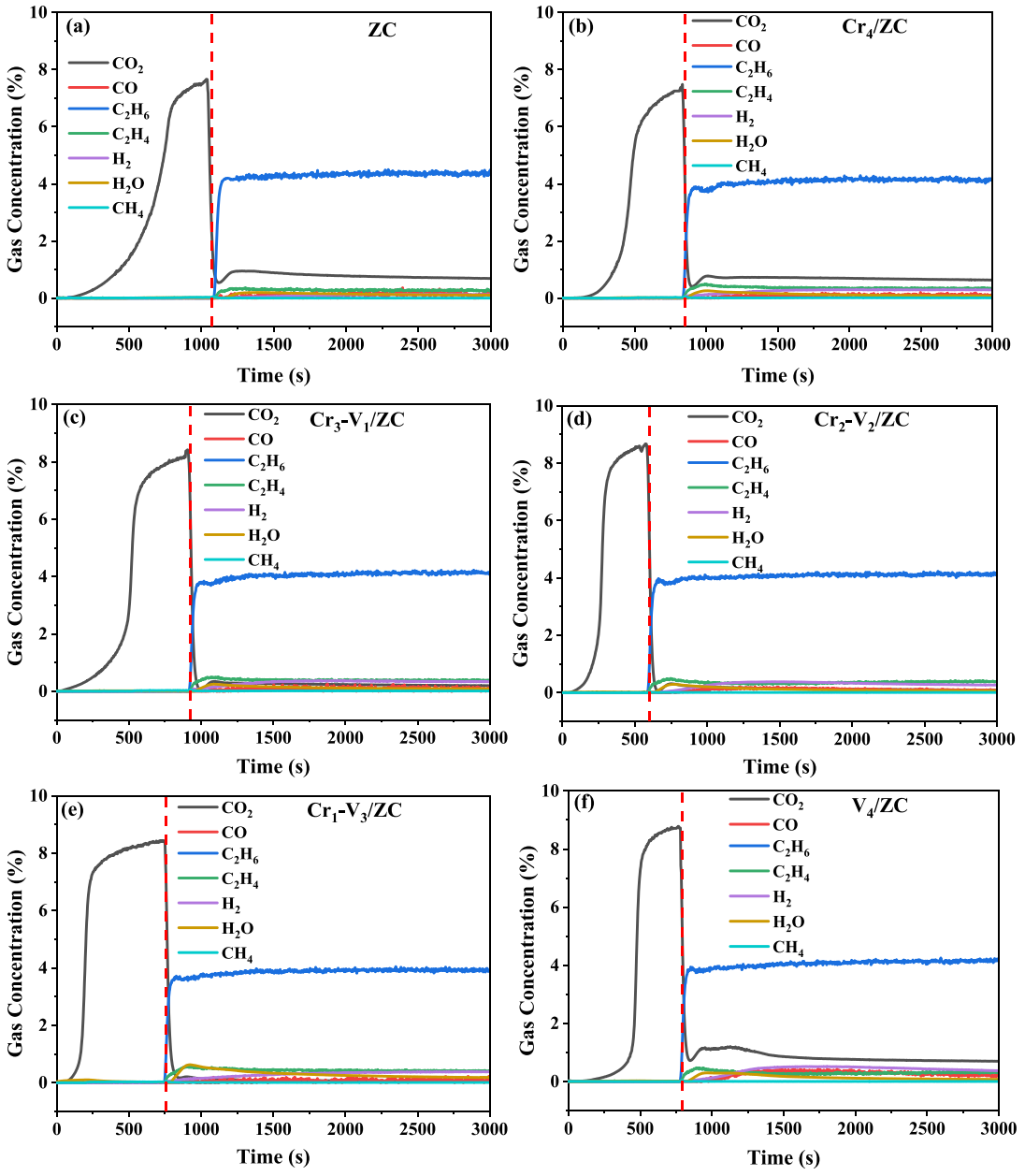

Figure 7. Adsorption−reaction (600−650 °C) profiles of (a) ZC, (b) Cr_4/ZC, (c) Cr_3-V_1/ZC, (d) Cr_2-V_2/ZC, (e) Cr_1-V_3/ZC, and (f) V_4/ZC structured monoliths.

Table 5. Summary of Adsorption-Reaction Results and Product Distribution over BFM Monoliths

monolith	CO_2 ads (mmol)	CO_2 des (mmol)	q_{ads} (mmol/g)	CO_2 con. %	C_2H_6 con. %	C_2H_4 S. %	C_2H_4 Y. %	syngas S. %	syngas Y. %	H_2/CO
ZC	1.30	0.43	2.60	66.90	14.30	44	5.60	36	4.60	0.87
Cr_4/ZC	1.04	0.39	2.08	62.66	18.42	46	7.53	41	7.20	1.77
Cr_3-V_1/ZC	0.82	0.33	1.64	59.75	18.93	43	7.50	44	7.57	1.93
Cr_2-V_2/ZC	0.83	0.33	1.66	60.24	18.80	43	7.75	44	7.90	1.98
Cr_1-V_3/ZC	0.86	0.31	1.72	63.95	22.40	42	8.11	45	8.80	2.18
V_4/ZC	1.11	0.40	2.22	63.96	18.90	29	6.94	59	8.60	2.25

and the synergetic effect between Cr and V.[53] In addition, in Table 4, the highest O^{2-}/OH^- ratio was obtained in Cr_1-V_3/ZC. It has been reported that the oxygenated species have a crucial role in the catalytic process of ODHE by activating the main reactions such as C_2H_6 dehydrogenation and dry reforming reactions.[53]

Direct Synthesis of Ethylene and Hydrogen from CO_2 and Ethane over BFM Monoliths. Using CO_2 as a soft oxidant in the ODHE is an attractive way to mitigate CO_2 emissions while simultaneously producing valuable products like ethylene and hydrogen. The synthesized BFM monoliths were assessed for combined CO_2 capture-utilization via the

https://doi.org/10.1021/acssuschemeng.2c05627
ACS Sustainable Chem. Eng. 2023, 11, 1006−1018

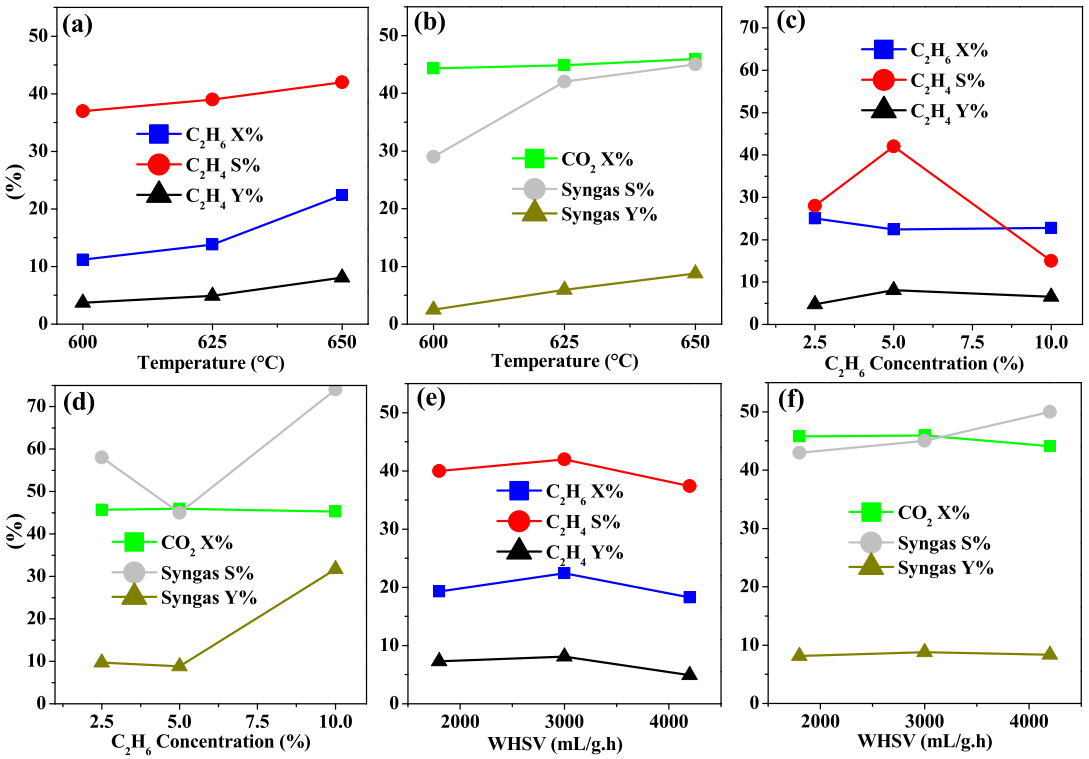

Figure 8. Effects of (a, b) reaction temperature, (c, d) C_2H_6 feed concentration, and (e, f) WHSV on products distribution over Cr_1-V_3/ZC monolith.

CO_2-ODHE reaction at an adsorption temperature of 600 °C, a reaction temperature of 650 °C, and a WHSV of 3000 mL/g·h, as illustrated in Figure 7a–f. The CO_2 adsorption capacity and product distribution results are listed in Table 5. The highest CO_2 capacity was found for ZC, which could have stemmed from its highest surface area, porosity, and higher degree of adsorption sites accessibility, compared when the adsorbent was mixed with the metal oxides (mono/bimetallic catalysts), as evidenced by the BET analysis. By a similar mechanism, combining the bare sample (ZC) with a single metal oxide such as Cr_4/ZC and V_4/ZC yielded a higher CO_2 uptake compared to bimetallic oxides such as Cr_1-V_3/ZC, Cr_3-V_1/ZC, and Cr_2-V_2/ZC. This observation can be explained by the less degree of CaO blockage by the single metal oxides relative to the bimetallic oxides. The reductions in CO_2 capacities translated into similar reductions in CO_2 conversions, which was expected because the amount of CO_2 utilized is a reflection of the amount captured. Hence, the degree to which CO_2 is available in the reaction step depends on the adsorption capacity.

In terms of catalytic activity, the samples displayed different behaviors. Nevertheless, the outlet gas stream revealed that C_2H_4, H_2, H_2O, and CO were the main products, representing the occurrence of C_2H_6 dehydrogenation and C_2H_6 reforming reactions with no C_2H_6 cracking as the amount of CH_4 deducted was negligible.[35] This can be confirmed from the atomic balances of C, H, and O for these reactions as the atomic balances ranged between ∼91 and 96 ± 3% for both reactions, indicating that most of the products were obtained from these reactions. The C_2H_4 and syngas (H_2 and CO) yields and selectivity were used to qualitatively determine the trend of products distribution, as shown in Table 5. ZC displayed the lowest catalytic activity, and product yield and selectivity due to the less catalytic active sites accessibility. The monometallic catalysts such as Cr_4/ZC and V_4/ZC displayed a similar C_2H_6 conversion at ∼18.5%; however, they revealed an opposite trend of product distribution. Cr_4/ZC was found to be more selective toward C_2H_4 by 31% higher than V_4/ZC. In contrast, V_4/ZC displayed a similar selectivity increase but to syngas. This implied that the reaction activity of C_2H_6 dehydrogenation was more feasible over Cr_4/ZC compared to V_4/ZC, which gives rise to the production of C_2H_4 more than hydrogen.[35] It is worth noting here that the H_2/CO ratio was higher than 1 in all samples, which can be attributed to the lower reaction temperature compared to the typical CO_2-ODHE reaction temperature (700 °C), as the reaction temperature of > 650 °C generally yields CO via the RWGS reaction.[32] This observation was further supported by the XPS data, in which Cr_4/ZC revealed a ∼60% increase in adsorptive oxygen species, whereas this percentage reduced upon increasing the content of V. The oxygen adsorption species, specially abundant OH^- species are known for their selectivity toward light olefins.[53] Furthermore, Cr^{6+}/Cr^{3+} ratio which plays a key role in promoting C_2H_4 production was relatively higher in Cr_4/ZC.[15]

The bimetallic catalysts in the developed BFM monoliths displayed activities between Cr_4/ZC and V_4/ZC as the single metal catalysts. This corresponded to the balanced oxygen species (lattice and adsorption) and the oxidative states of Cr and V, as evidenced by the XPS results. With this being the case, Cr-V/ZC samples contributed to the production of C_2H_4 and syngas via the bond cleavage of C–H and C–C in the C_2H_6 dehydrogenation and C_2H_6 reforming reactions, respectively. However, Cr_1-V_3/ZC exhibited the highest catalytic activity among all samples, with 22.4% C_2H_6 conversion, and 8.11 and 8.80% C_2H_4 and syngas yields, respectively. It can be concluded that the Cr-based sample was more selective toward C_2H_4 via the C_2H_6 dehydrogenation

https://doi.org/10.1021/acssuschemeng.2c05627
ACS Sustainable Chem. Eng. 2023, 11, 1006–1018

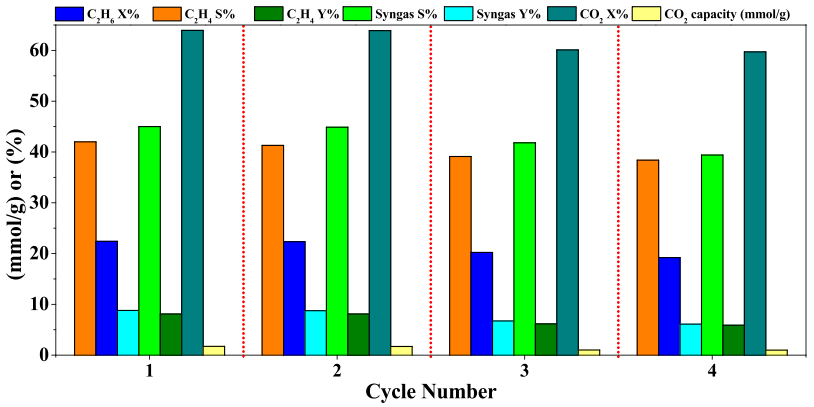

Figure 9. Cyclic experiments (adsorption−reaction) of the Cr_1-V_3/ZC monolith at 600−650 °C, 3000 mL/g·h WHSV, 10% CO_2/Ar, and 5% C_2H_6/Ar.

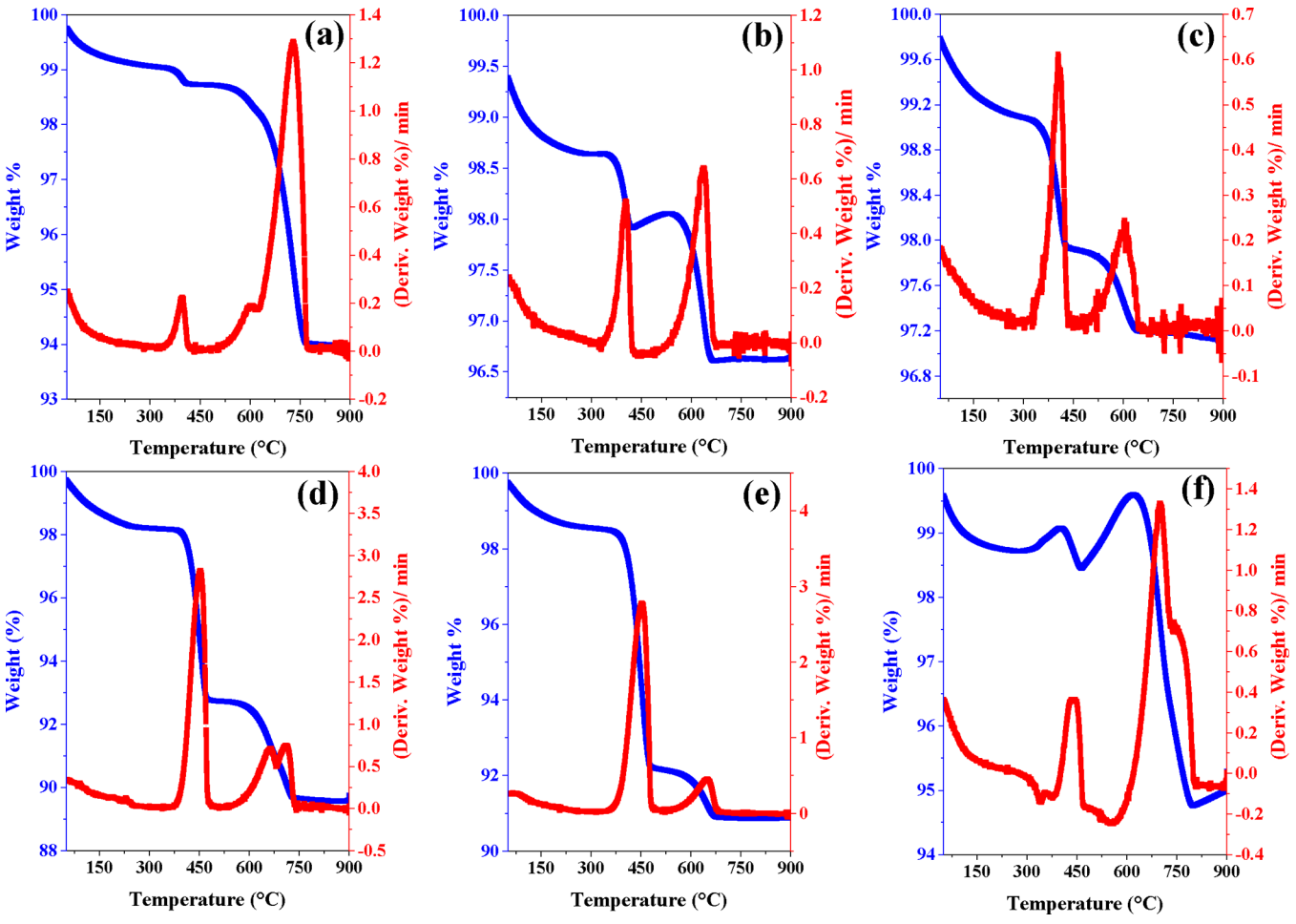

Figure 10. Thermogravimetric analysis of (a) ZC, (b) Cr_4/ZC, (c) Cr_3-V_1/ZC, (d) Cr_2-V_2/ZC, (e) Cr_1-V_3/ZC, and (f) V_4/ZC monoliths.

reaction, and the Cr-V/V-based samples increased the catalytic activity in a balanced manner between C_2H_4 and syngas with a relatively enhanced activity toward C−C bond cleavage via the C_2H_6 reforming reaction for syngas production.

Comparing the performance of the Cr_1-V_3/ZC BFM monolith to literature data reported for the CO_2-ODHE reaction, the developed BFM displayed comparable performance to most of the materials. For example, CO_2 and C_2H_6 conversions and C_2H_4 selectivity of 9.3, 9.9, and 80.4%, respectively, were reported for Pd-Fe/CeO_2 at 650 °C,[54] which were lower than those observed here for CO_2 and C_2H_6 conversions and higher than C_2H_4 selectivity. Ga/TiSi-3, in another study,[55] displayed better catalytic performance than Cr_1-V_3/ZC, particularly for C_2H_6 conversion and C_2H_4 selectivity, but it showed lower CO_2 conversion compared to Cr_1-V_3/ZC. Generally, by looking at the studies reported in Table S2, the Cr_1-V_3/ZC BFM monolith showed an acceptable catalytic performance and outperformed many other materials reported in Table S2, indicating that the bimetallic BFMs can

https://doi.org/10.1021/acssuschemeng.2c05627
ACS Sustainable Chem. Eng. 2023, 11, 1006−1018

be manufactured into monolithic contactors without significant malfunctions or effects on their catalytic activity.

To better assess the ODHE performance of the BFM monoliths, the process conditions (reaction temperature, ethane feed concentration, and WHSV) were systematically varied over the Cr_1-V_3/ZC sample, and the results are presented in Figure 8a–f. First looking at the effect of reaction temperature (Figure 8a,b), it is obvious that increasing the reaction temperature resulted in a higher catalytic activity as the C_2H_6 conversion and C_2H_4 and syngas yields and selectivities were all increased. This indicated that increasing the reaction temperature within the range of 600–650 °C led to desirable C_2H_6 dehydrogenation and reforming mechanisms but did not lead to a thermodynamic shift toward thermal cracking reactions.[2,10] To assess the effect of C_2H_6 concentration (Figure 8c,d), the reaction temperature and WHSV were held constant at 650 °C and 3000 mL/g·h, respectively. Increasing the ethane concentration led to a significant decline in C_2H_4 selectivity from 43% at 5% C_2H_6 feed concentration to 14% when the C_2H_6 feed concentration was elevated to 10%. However, the syngas selectivity was clearly increased (e.g., CO = 21% and H_2 = 54% at 10% C_2H_6 feed concentration, as shown in Figure S1). With this being the case, the C_2H_6 reforming reaction was the main reaction due to the breakage of the C–C bond at high C_2H_6 feed concentrations, as this reaction is known to increase the selectivity of syngas.[56] Similarly, increasing the WHSV of the feed consistently led to decline in all reactants conversions, C_2H_4 yield, and C_2H_4 selectivity; however, there was a slight increase in the syngas yield and selectivity (Figure 8e,f). T enhanced syngas selectivity and yield at high WHSV could be attributed to other cracking reactions such as direct C_2H_6 cracking into C_2H_4 and H_2 and, subsequently, H_2 reaction with CO_2 to produce CO via the RWGA reaction, in which these reactions are mostly producing H_2 due to a lower feasibility of RWGS reaction, as discussed previously. This mechanism was expected because the effect of reaction temperature did not shift the equilibrium to thermal cracking toward CH_4, as shown in Figure 8a,b, and the catalytic activity was enhanced for both C_2H_4 and syngas, indicating the feasibility of the C_2H_6 dehydrogenation and reforming reactions and not the C_2H_6 cracking reaction to CH_4.[40] It can be reasonably concluded that the decline in catalytic activity toward C_2H_4 due to a high WHSV were due to thermal cracking but mostly stemmed from insufficient contact time between the catalytic surface and the feed stream. Cr_1-V_3/ZC displayed its best overall performance at 650 °C, 3000 mL/g·h WHSV, and 5% feed concentration, as this set of conditions generated the best balance between C_2H_4/syngas yields and reactants conversions.

To determine the long-term stability of the Cr_1-V_3/ZC monolith, four adsorption–reaction cycles were carried out at 650 °C, as shown in Figure 9. As is evident, the BFM monolith exhibited relatively stable performance across the four cycles, which could be attributed to a low degree of coke formation during the reaction step. The low coke formation can be either due to the oxygen species availability or the occurrence of Boudouard reaction.[7] To quantify the coke residuals on the developed BFMs, thermogravimetric analysis (TGA) was performed on all the samples after one cycle of adsorption–reaction, and the results are presented in Figure 10a–f. The TGA profiles displayed two main peaks, one below 470 °C, which was related to the $Ca(OH)_2$ decomposition to CaO and water, and another one between 500 and 750 °C, which was attributed to the coke formation.[15,57] The latter peak intensity was smaller in the bimetallic samples (Cr-V/ZC), while it was more intense in the bare and monometallic samples (ZC, Cr, or V/ZC), confirming the role of metal interactions in reducing the coke formation to maintain the catalytic activity due to oxygen species availability.[58] This was also supported by the coke quantifications provided in Table S1, as the coke formation was reduced form 18.13 mg_{coke}/g for the bare sample (ZC) to 16.92 mg_{coke}/g as the average value when the bimetallic catalyst was used (Cr-V/ZC). After four cycles, the coke formation peak was increased compared to one cycle (Figure S2); however, Cr_1-V_3/ZC was active and stable across the two cycles and was slightly affected by the coke deposition across the third and fourth cycles, as shown in Figure 9.

Figure 11 shows the Raman spectra of fresh and spent Cr_1-V_3/ZC samples. It can be seen that all the Cr_1-V_3/ZC

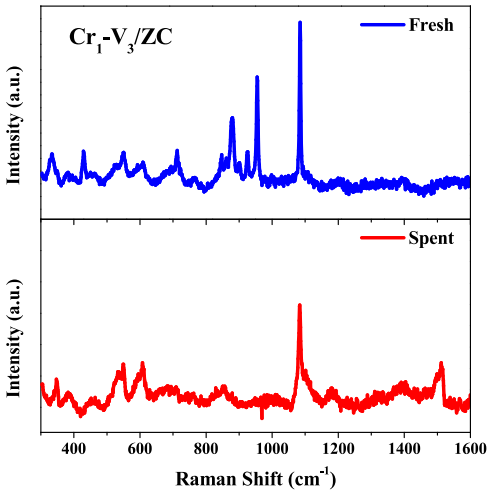

Figure 11. Raman spectra of fresh and spent Cr_1-V_3/ZC samples.

precursors were identified by Raman spectroscopy at 380, 550.7, 800–1000, and 1084.6 cm^{-1}, which corresponded to ZSM-5,[59] Cr_2O_3 crystallites,[60] Cr and V species,[61,62] and CaO,[63] respectively. V_2O_5 also displayed characteristic bands at 515 and 705 cm^{-1}.[64] However, the intensity of these peaks was reduced after four cycles of adsorption–reaction in the spent sample, which could be attributed to the coke formation. This can be confirmed by the appearance of a peak between 1484 and 1520 cm^{-1} in the spectrum of the spent sample, which arised fromin-plane stretching of sp^2 carbons of olefins, forming structured coke or graphite-like structures.[65] However, this peak was minor and had low intensity, in agreement with the coke quantification analysis discussed earlier, as the coke formed had a minor effect on the catalytic activity.

CONCLUSIONS

A primary objective of this proof-of-concept study was to establish the feasibility and rationale for formulation, processing, and shape engineering of structured BFM monoliths containing CaO adsorbent admixed with Cr_2O_3-V_2O_5/ZSM-5 catalysts. The Cr_2O_3 and V_2O_5 metal oxides ratios were optimized, and the effects of monometallic and bimetallic phases on the stability and performance of the structured BFMs were systematically investigated. The findings indicated that the bimetallic catalyst in the developed BFMs,

https://doi.org/10.1021/acssuschemeng.2c05627
ACS Sustainable Chem. Eng. 2023, 11, 1006–1018

namely, Cr_1-V_3/ZC, can lead to improved catalytic and adsorptive performances compared to the monometallic catalysts such as Cr_4/ZC and V_4/ZC. Increasing the V content within BFM monoliths gave rise to enhancement in the catalytic activity toward hydrogen (syngas) production *via* the C_2H_6 reforming reaction, whereas high Cr contents led to enhanced C_2H_4 production, which was ascribed to the C_2H_6 dehydrogenation reaction. This study provides a clear understanding of cooperative and bifunctional material design for *in situ* CO_2 capture−utilization and simultaneous production of ethylene and hydrogen in a single bed.

■ ASSOCIATED CONTENT

Supporting Information

The Supporting Information is available free of charge at https://pubs.acs.org/doi/10.1021/acssuschemeng.2c05627.

Estimation of adsorption−reaction, coke formation quantifications after *in situ* CO_2 capture−conversion in simultaneous ethane dehydrogenation/reforming reactions, comparing the *in situ* CO_2 capture−conversion performance in the Cr_1-V_3/ZC monolith with the open literature, effect of reaction temperature, C_2H_6 feed concentration, and WHSV on product distribution over Cr_1-V_3/ZC, and thermogravimetric analysis of Cr_1-V_3/ZC after four cycles of adsorption−reaction (PDF)

■ AUTHOR INFORMATION

Corresponding Authors

Ali A. Rownaghi − *Department of Chemistry, Cleveland State University, Cleveland, Ohio 44115, United States;* orcid.org/0000-0001-5228-5624; Email: a.rownaghi@csuohio.edu

Fateme Rezaei − *Linda and Bipin Doshi Department of Chemical and Biochemical Engineering, Missouri University of Science and Technology, Rolla, Missouri 65409, United States;* orcid.org/0000-0002-4214-4235; Email: rezaeif@mst.edu

Author

Khaled Baamran − *Linda and Bipin Doshi Department of Chemical and Biochemical Engineering, Missouri University of Science and Technology, Rolla, Missouri 65409, United States*

Complete contact information is available at: https://pubs.acs.org/10.1021/acssuschemeng.2c05627

Notes

The authors declare no competing financial interest.

■ ACKNOWLEDGMENTS

The authors acknowledge the National Science Foundation internship program (NSF CBET-1802049) and the Electron Microscopy Core (EMC) at the University of Missouri Columbia for performing the SEM and EDS characterizations. The authors also acknowledge the Materials Research Center (MRC) at Missouri University of Science and Technology for performing the XRD and XPS characterizations.

■ REFERENCES

(1) Torres Galvis, H. M.; de Jong, K. P. Catalysts for Production of Lower Olefins from Synthesis Gas: A Review. *ACS Catal.* **2013**, *3*, 2130−2149.

(2) Liu, J.; He, N.; Zhang, Z.; Yang, J.; Jiang, X.; Zhang, Z.; Su, J.; Shu, M.; Si, R.; Xiong, G.; Xie, H. B.; Vilé, G. Highly-Dispersed Zinc Species on Zeolites for the Continuous and Selective Dehydrogenation of Ethane with CO_2 as a Soft Oxidant. *ACS Catal.* **2021**, *11*, 2819−2830.

(3) Baamran, K.; Newport, K.; Rownaghi, A. A.; Rezaei, F. Development and Assessment of Magnetic Fe_2O_3@MOF-74 Composite Sorbents for Ethylene/Ethane Separation. *Chem. Eng. J.* **2023**, *451*, No. 139006.

(4) Gao, Y.; Haeri, F.; He, F.; Li, F. Alkali Metal-Promoted $La_xSr_{2-x}FeO_{4-\delta}$ Redox Catalysts for Chemical Looping Oxidative Dehydrogenation of Ethane. *ACS Catal.* **2018**, *8*, 1757−1766.

(5) Galvita, V.; Siddiqi, G.; Sun, P.; Bell, A. T. Ethane Dehydrogenation on Pt/Mg(Al)O and Ptsn/Mg(Al)O Catalysts. *J. Catal.* **2010**, *271*, 209−219.

(6) Sattler, J. J. H. B.; Ruiz-Martinez, J.; Santillan-Jimenez, E.; Weckhuysen, B. M. Catalytic Dehydrogenation of Light Alkanes on Metals and Metal Oxides. *Chem. Rev.* **2014**, *114*, 10613−10653.

(7) Theofanidis, S. A.; Loizidis, C.; Heracleous, E.; Lemonidou, A. A. CO_2-Oxidative Ethane Dehydrogenation over Highly Efficient Carbon-Resistant Fe-Catalysts. *J. Catal.* **2020**, *388*, 52−65.

(8) Porosoff, M. D.; Myint, M. N. Z.; Kattel, S.; Xie, Z.; Gomez, E.; Liu, P.; Chen, J. G. Identifying Different Types of Catalysts for CO_2 Reduction by Ethane through Dry Reforming and Oxidative Dehydrogenation. *Angew. Chem., Int. Ed.* **2015**, *54*, 15501−15505.

(9) Al-Mamoori, A.; Rownaghi, A. A.; Rezaei, F. Combined Capture and Utilization of CO_2 for Syngas Production over Dual-Function Materials. *ACS Sustainable Chem. Eng.* **2018**, *6*, 13551−13561.

(10) Jalid, F.; Khan, T. S.; Haider, M. A. CO_2 Reduction and Ethane Dehydrogenation on Transition Metal Catalysts: Mechanistic Insights, Reactivity Trends and Rational Design of Bimetallic Alloys. *Catal. Sci. Technol.* **2021**, *11*, 97−115.

(11) Al-Mamoori, A.; Krishnamurthy, A.; Rownaghi, A. A.; Rezaei, F. Carbon Capture and Utilization Update. *Energy Technol.* **2017**, *5*, 834−849.

(12) Gomez, E.; Yan, B.; Kattel, S.; Chen, J. G. Carbon Dioxide Reduction in Tandem with Light-Alkane Dehydrogenation. *Nat. Rev. Chem.* **2019**, *3*, 638−649.

(13) Kattel, S.; Chen, J. G.; Liu, P. Mechanistic Study of Dry Reforming of Ethane by CO_2 on a Bimetallic PtNi(111) Model Surface. *Catal. Sci. Technol.* **2018**, *8*, 3748−3758.

(14) Han, Y.; Wang, Z.; Han, X.; Fang, W.; Zhou, Y.; Lei, K.; You, B.; Park, H. S.; Xia, B. Y. Selectively Converting Carbon Dioxide to Syngas over Intermetallic AuCu Catalysts. *ACS Sustainable Chem. Eng.* **2021**, *9*, 2609−2615.

(15) Al-Mamoori, A.; Lawson, S.; Rownaghi, A. A.; Rezaei, F. Oxidative Dehydrogenation of Ethane to Ethylene in an Integrated CO_2 Capture-Utilization Process. *Appl. Catal., B* **2020**, *278*, No. 119329.

(16) Kosaka, F.; Liu, Y.; Chen, S.-Y.; Mochizuki, T.; Takagi, H.; Urakawa, A.; Kuramoto, K. Enhanced Activity of Integrated CO_2 Capture and Reduction to CH_4 under Pressurized Conditions toward Atmospheric CO_2 Utilization. *ACS Sustainable Chem. Eng.* **2021**, *9*, 3452−3463.

(17) Lawson, S.; Baamran, K.; Newport, K.; Garcia, E.; Jacobs, G.; Rezaei, F.; Rownaghi, A. A. Adsorption-Enhanced Bifunctional Catalysts for In-situ CO_2 Capture and Utilization in Propylene Production: A Proof-of-Concept Study. *ACS Catal.* **2022**, *12*, 14264−14279.

(18) Atanga, M. A.; Rezaei, F.; Jawad, A.; Fitch, M.; Rownaghi, A. A. Oxidative Dehydrogenation of Propane to Propylene with Carbon Dioxide. *Appl. Catal., B* **2018**, *220*, 429−445.

(19) Jeong-Potter, C.; Farrauto, R. Feasibility Study of Combining Direct Air Capture of CO_2 and Methanation at Isothermal Conditions with Dual Function Materials. *Appl. Catal., B* **2021**, *282*, No. 119416.

(20) Huang, J.; Jiang, S.; Wang, M.; Wang, X.; Gao, J.; Song, C. Dynamic Evolution of Fe and Carbon Species over Different ZrO_2 Supports during CO Prereduction and Their Effects on CO_2

Hydrogenation to Light Olefins. *ACS Sustainable Chem. Eng.* **2021**, *9*, 7891−7903.
(21) Berger, A. H.; Bhown, A. S. Comparing Physisorption and Chemisorption Solid Sorbents for Use Separating CO_2 from Flue Gas Using Temperature Swing Adsorption. *Energy Procedia* **2011**, *4*, 562−567.
(22) Park, S. J.; Bukhovko, M. P.; Jones, C. W. Integrated Capture and Conversion of CO_2 into Methane Using $NaNO_3$/MgO+ Ru/Al_2O_3 as a Catalytic Sorbent. *Chem. Eng. J.* **2021**, *420*, No. 130369.
(23) Alghamdi, T.; Baamran, K. S.; Okoronkwo, M. U.; Rownaghi, A. A.; Rezaei, F. Metal-Doped K−Ca Double Salts with Improved Capture Performance and Stability for High-Temperature CO_2 Adsorption. *Energy Fuels* **2021**, *35*, 4258−4266.
(24) Al-Mamoori, A.; Alghamdi, T.; Rownaghi, A. A.; Rezaei, F. Enhancing the Ethylene Yield over Hybrid Adsorbent Catalyst Materials in CO_2-Assisted Oxidative Dehydrogenation of Ethane by Tuning Catalyst Support Properties. *Energy Fuels* **2020**, *34*, 14483−14492.
(25) Lawson, S.; Farsad, A.; Rezaei, F.; Ludlow, D.; Rownaghi, A. A. Direct Ink Writing of Metal Oxide/H-ZSM-5 Catalysts for *n*-Hexane Cracking: A New Method of Additive Manufacturing with High Metal Oxide Loading. *ACS Appl. Mater. Interfaces* **2021**, *13*, 781−794.
(26) Magzoub, F.; Li, X.; Lawson, S.; Rezaei, F.; Rownaghi, A. A. 3D-Printed HZSM-5 and 3D-HZM5@SAPO-34 Structured Monoliths with Controlled Acidity and Porosity for Conversion of Methanol to Dimethyl Either. *Fuel* **2020**, *280*, No. 118628.
(27) Lawson, S.; Newport, K. A.; Axtell, A.; Boucher, C.; Grant, B.; Haas, M.; Lee, M.; Rezaei, F.; Rownaghi, A. A. Structured Bifunctional Catalysts for CO_2 Activation and Oxidative Dehydrogenation of Propane. *ACS Sustainable Chem. Eng.* **2021**, *9*, 5716−5727.
(28) Lawson, S.; Li, X.; Thakkar, H.; Rownaghi, A. A.; Rezaei, F. Recent Advances in 3D Printing of Structured Materials for Adsorption and Catalysis Applications. *Chem. Rev.* **2021**, *121*, 6246−6291.
(29) Magzoub, F.; Lawson, S.; Rezaei, F.; Rownaghi, A. A. Directly Printed Oxide/ZSM-5 Bifunctional Catalysts for Methanol Conversion to Dimethyl Ether with Exceptional Stability, Conversion, and Selectivity. *Energy Fuels* **2021**, *35*, 2619−2629.
(30) Lawson, S.; Farsad, A.; Adebayo, B.; Newport, K.; Schueddig, K.; Lowrey, E.; Polo-Garzon, F.; Rezaei, F.; Rownaghi, A. A. A Novel Method of 3D Printing High-Loaded Oxide/H-ZSM-5 Catalyst Monoliths for Carbon Dioxide Reduction in Tandem with Propane Dehydrogenation. *Adv. Sustainable Syst.* **2021**, *5*, No. 2000257.
(31) Lawson, S.; Baamran, K.; Newport, K.; Rezaei, F.; Rownaghi, A. Screening of Adsorbent/Catalyst Composite Monoliths for Carbon Capture-Utilization and Ethylene Production. *ACS Appl. Mater. Interfaces* **2021**, *13*, 55198−55207.
(32) Baamran, K.; Lawson, S.; Rownaghi, A. A.; Rezaei, F. Process Evaluation and Kinetic Analysis of 3D-Printed Monoliths Comprised of CaO and Cr/H-ZSM-5 in Combined CO_2 Capture-C_2H_6 Oxidative Dehydrogenation to C_2H_4. *Chem. Eng. J.* **2022**, *435*, No. 134706.
(33) Baena-Moreno, F. M.; González-Castaño, M.; Navarro de Miguel, J. C.; Miah, K. U. M.; Ossenbrink, R.; Odriozola, J. A.; Arellano-Garcia, H. Stepping toward Efficient Microreactors for CO_2 Methanation: 3D-Printed Gyroid Geometry. *ACS Sustainable Chem. Eng.* **2021**, *9*, 8198−8206.
(34) Arellano-Trevino, M. A.; Kanani, N.; Jeong-Potter, C. W.; Farrauto, R. J. Bimetallic Catalysts for CO_2 Capture and Hydrogenation at Simulated Flue Gas Conditions. *Chem. Eng. J.* **2019**, *375*, No. 121953.
(35) Numan, M.; Eom, E.; Li, A.; Mazur, M.; Cha, H. W.; Ham, H. C.; Jo, C.; Park, S.-E. Oxidative Dehydrogenation of Ethane with CO_2 as a Soft Oxidant over a PtCe Bimetallic Catalyst. *ACS Catal.* **2021**, *11*, 9221−9232.
(36) Sankar, M.; Dimitratos, N.; Miedziak, P. J.; Wells, P. P.; Kielye, C. J.; Hutchings, G. J. Designing Bimetallic Catalysts for a Green and Sustainable Future. *Chem. Soc. Rev.* **2012**, *41*, 8099−8139.
(37) Myint, M.; Yan, B.; Wan, J.; Zhao, S.; Chen, J. G. Reforming and Oxidative Dehydrogenation of Ethane with CO_2 as a Soft Oxidant over Bimetallic Catalysts. *J. Catal.* **2016**, *343*, 168−177.
(38) Ryoo, R.; Kim, J.; Jo, C.; Han, S. W.; Kim, J.-C.; Park, H.; Han, J.; Shin, H. S.; Shin, J. W. Rare-Earth−Platinum Alloy Nanoparticles in Mesoporous Zeolite for Catalysis. *Nature* **2020**, *585*, 221−224.
(39) Lawson, S.; Baamran, K.; Newport, K.; Alghamadi, T.; Jacobs, G.; Rezaei, F.; Rownaghi, A. A. Integrated Direct Air Capture and Oxidative Dehydrogenation of Propane with CO_2 at Isothermal Conditions. *Appl. Catal., B* **2022**, *303*, No. 120907.
(40) Lawson, S.; Baamran, K.; Newport, K.; Rezaei, F.; Rownaghi, A. A. Formulation and Processing of Dual Functional Adsorbent/Catalyst Structured Monoliths Using an Additively Manufactured Contactor for Direct Capture/Conversion of CO_2 with Cogeneration of Ethylene. *Chem. Eng. J.* **2022**, *431*, No. 133224.
(41) Ambroz, F.; Macdonald, T. J.; Martis, V.; Parkin, I. P. Evaluation of the BET Theory for the Characterization of Meso and Microporous MOFs. *Small methods* **2018**, *2*, No. 1800173.
(42) Thommes, M.; Kaneko, K.; Neimark, A. V.; Olivier, J. P.; Rodriguez-Reinoso, F.; Rouquerol, J.; Sing, K. S. W. Physisorption of Gases, with Special Reference to the Evaluation of Surface Area and Pore Size Distribution (IUPAC Technical Report). *Pure Appl. Chem.* **2015**, *87*, 1051−1069.
(43) Yurdakal, S.; Garlisi, C.; Özcan, L.; Bellardita, M.; Palmisano, G. (Photo)catalyst Characterization Techniques. In *Heterogeneous photocatalysis*; Elsevier, 2019; pp. 87−152, DOI: DOI: 10.1016/B978-0-444-64015-4.00004-3.
(44) Tompsett, G. A.; Krogh, L.; Griffin, D. W.; Conner, W. C. Hysteresis and Scanning Behavior of Mesoporous Molecular Sieves. *Langmuir* **2005**, *21*, 8214−8225.
(45) Jansen, J. C.; van der Gaag, F. J.; van Bekkum, H. Identification of ZSM-Type and Other 5-Ring Containing Zeolites by i.r. Spectroscopy. *Zeolites* **1984**, *4*, 369−372.
(46) Li, X.; Alwakwak, A. A.; Rezaei, F.; Rownaghi, A. A. Synthesis of Cr, Cu, Ni, and Y-Doped 3D-Printed ZSM-5 Monoliths and Their Catalytic Performance for *n*-Hexane Cracking. *ACS Appl. Energy Mater.* **2018**, *1*, 2740−2748.
(47) Allahyari, S.; Haghighi, M.; Ebadi, A.; Hosseinzadeh, S. Ultrasound Assisted Co-Precipitation of Nanostructured CuO-ZnO-Al_2O_3 over HZSM-5: Effect of Precursor and Irradiation Power on Nanocatalyst Properties and Catalytic Performance for Direct Syngas to DME. *Ultrason. Sonochem.* **2014**, *21*, 663−673.
(48) Martínez, M. L.; Gómez Costa, M. B.; Monti, G. A.; Anunziata, O. A. Synthesis, Characterization and Catalytic Activity of AlSBA-3 Mesoporous Catalyst Having Variable Silicon-to-Aluminum Ratios. *Microporous Mesoporous Mater.* **2011**, *144*, 183−190.
(49) Mirghiasi, Z.; Bakhtiari, F.; Darezereshki, E.; Esmaeilzadeh, E. Preparation and Characterization of CaO Nanoparticles from $Ca(OH)_2$ by Direct Thermal Decomposition Method. *J. Ind. Eng. Chem.* **2014**, *20*, 113−117.
(50) Li, J.; Xiao, G.; Guo, Z.; Lin, B.; Hu, Y.; Fu, M.; Ye, D. ZSM-5-Supported V-Cu Bimetallic Oxide Catalyst for Remarkable Catalytic Oxidation of Toluene in Coal-Fired Flue Gas. *Chem. Eng. J.* **2021**, *419*, No. 129675.
(51) Kadari, A.; Schemme, T.; Kadri, D.; Wollschläger, J. XPS and Morphological Properties of Cr_2O_3 Thin Films Grown by Thermal Evaporation Method. *Results Phys.* **2017**, *7*, 3124−3129.
(52) Ali, A. A.; Madkour, M.; Al Sagheer, F.; Zaki, M. I.; Abdel Nazeer, A. Low-Temperature Catalytic CO Oxidation over Non-Noble, Efficient Chromia in Reduced Graphene Oxide and Graphene Oxide Nanocomposites. *Catalysts* **2020**, *10*, 105.
(53) Fonzeu Monguen, C. K.; El Kasmi, A.; Arshad, M. F.; Kouotou, P. M.; Daniel, S.; Tian, Z. Y. Oxidative Dehydrogenation of Propane into Propene over Chromium Oxides. *Ind. Eng. Chem. Res.* **2022**, *61*, 4546−4560.
(54) Li, X.; Yang, Z.; Zhang, L.; He, Z.; Fang, R.; Wang, Z.; Yan, Y.; Ran, J. Effect of Pd Doping in (Fe/Ni)/CeO_2 Catalyst for the Reaction Path in CO_2 Oxidative Ethane Dehydrogenation/Reforming. *Energy* **2021**, *234*, No. 121261.

(55) Lei, T.; Cheng, Y.; Miao, C.; Hua, W.; Yue, Y.; Gao, Z. Silica-Doped TiO2 as Support of Gallium Oxide for Dehydrogenation of Ethane with CO_2. *Fuel Process. Technol.* **2018**, *177*, 246−254.
(56) Najari, S.; Saeidi, S.; Concepcion, P.; Dionysiou, D. D.; Bhargava, S. K.; Lee, A. F.; Wilson, K. Oxidative Dehydrogenation of Ethane: Catalytic and Mechanistic Aspects and Future Trends. *Chem. Soc. Rev.* **2021**, *50*, 4564−4605.
(57) Al-Mamoori, A.; Lawson, S.; Rownaghi, A. A.; Rezaei, F. Improving Adsorptive Performance of CaO for High-Temperature CO_2 Capture through Fe and Ga Doping. *Energy Fuels* **2019**, *33*, 1404−1413.
(58) Xie, Z.; Tian, D.; Xie, M.; Yang, S.-Z.; Xu, Y.; Rui, N.; Lee, J. H.; Senanayake, S. D.; Li, K.; Wang, H.; Kattel, S.; Chen, J. G. Interfacial Active Sites for CO_2 Assisted Selective Cleavage of C−C/C−H Bonds in Ethane. *Chem* **2020**, *6*, 2703−2716.
(59) An, H.; Zhang, F.; Guan, Z.; Liu, X.; Fan, F.; Li, C. Investigating the Coke Formation Mechanism of H-ZSM-5 during Methanol Dehydration Using Operando UV−Raman Spectroscopy. *ACS Catal.* **2018**, *8*, 9207−9215.
(60) Zhang, F.; Wu, R.; Yue, Y.; Yang, W.; Gu, S.; Miao, C.; Hua, W.; Gao, Z. Chromium Oxide Supported on ZSM-5 as a Novel Efficient Catalyst for Dehydrogenation of Propane with CO_2. *Microporous Mesoporous Mater.* **2011**, *145*, 194−199.
(61) Baddour-Hadjean, R.; Raekelboom, E.; Pereira-Ramos, J. P. New Structural Characterization of the $Li_xV_2O_5$ System Provided by Raman Spectroscopy. *Chem. Mater.* **2006**, *18*, 3548−3556.
(62) Cheng, Y.; Zhang, F.; Zhang, Y.; Miao, C.; Hua, W.; Yue, Y.; Gao, Z. Oxidative Dehydrogenation of Ethane with CO_2 over Cr Supported on Submicron ZSM-5 Zeolite. *Chin. J. Catal.* **2015**, *36*, 1242−1248.
(63) Rownaghi, A. A. .; Huhnke, R. L. Producing hydrogen-rich gases by steam reforming of syngas tar over CaO/MgO/NiO catalysts. *ACS Sustainable Chem. Eng.* **2013**, *1*, 80−86.
(64) Mohan, H.; Lim, J.-M.; Lee, S.-W.; Cho, M.; Park, Y.-J.; Seralathan, K.-K.; Oh, B.-T. V_2O_5/RGO/Pt Nanocomposite on Oxytetracycline Degradation and Pharmaceutical Effluent Detoxification. *J. Chem. Technol. Biotechnol.* **2020**, *95*, 297−307.
(65) Castano, P.; Elordi, G.; Olazar, M.; Aguayo, A. T.; Pawelec, B.; Bilbao, J. Insights into the Coke Deposited on HZSM-5, Hβ and HY Zeolites during the Cracking of Polyethylene. *Appl. Catal., B* **2011**, *104*, 91−100.